

POPULATION DIAGRAM ANALYSIS OF MOLECULAR LINE EMISSION

PAUL F. GOLDSMITH

National Astronomy and Ionosphere Center, Department of Astronomy, Cornell University, Ithaca NY 14853; pfg@astrosun.tn.cornell.edu

AND

WILLIAM D. LANGER

MS 169-506, Jet Propulsion Laboratory, California Institute of Technology, Pasadena CA 91109; langer@nimba.jpl.nasa.gov

Received 1998 October 26; accepted 1998 December 29

ABSTRACT

We develop the use of the population diagram method to analyze molecular emission in order to derive physical properties of interstellar clouds. We focus particular attention on how the optical depth affects the derived total column density and the temperature. We derive an optical depth correction factor that can be evaluated based on observations and that incorporates the effect of saturation on derived upper level populations. We present analytic results for linear molecules in local thermodynamic equilibrium (LTE). We investigate numerically how subthermal excitation influences the population diagram technique, studying how the determination of kinetic temperature is affected when the local density is insufficient to achieve LTE. We present results for HC_3N and CH_3OH , representative of linear and nonlinear molecules, respectively. In some cases, alternative interpretations to the standard optically thin and thermalized picture yield significantly different results for column density and kinetic temperature, and we discuss this behavior. The population diagram method can be a very powerful tool for determining physical conditions in dense clouds if proper recognition is given to effects of saturation and subthermal excitation. We argue that the population diagram technique is, in fact, superior to fitting intensities of different transitions directly, and we indicate how it can be effectively employed.

Subject headings: ISM: clouds — ISM: molecules — radiative transfer

1. INTRODUCTION

Molecular line emission can yield important information about physical conditions in dense interstellar clouds. The column density of the species being observed and the cloud kinetic temperature can most straightforwardly be determined; indeed, under certain conditions, these parameters can be obtained from observation of a single transition. Other important characteristics of clouds, such as their density, velocity structure, and the magnetic field distribution, can be obtained only by observing multiple transitions, making maps, or employing specialized types of observations.

However, the validity of even the apparently simpler techniques needs to be demonstrated. For example, a single transition, if optically thick and thermalized, can provide the kinetic temperature (T_K) of the gas at a location in the cloud where $\tau \simeq 1$. In the case of carbon monoxide, the optical depth of the common isotopic species can be checked by observing rarer isotopomers, while the thermalization can be evaluated by an approximate comparison of density (determined from a different technique) with the relatively low spontaneous decay rates of the lower rotational transitions. The confidence developed in this approach has led to the widespread use of ^{12}CO as a probe of the kinetic temperature in molecular clouds. It is useful in this application, even though observational results as well as theoretical models suggest that there are significant variations of the kinetic temperature as a function of position within molecular clouds.

An optically thin transition produces an antenna temperature that is proportional to the column density in the upper level of the transition being observed, and if all transitions are thermalized and we know the kinetic temperature, we can convert the single measured column density into the column density of the species in ques-

tion. Some of the early spectral surveys of emission from molecular clouds provided the first instance in which a sufficient number of transitions were observed that an analysis of the excitation, or at least a check for self-consistency of the assumptions of optical thinness and thermalization, was possible.

One potentially important and frequently adopted technique to analyze cloud properties from molecular line emission is the “rotation diagram.” This term refers to a plot of the column density per statistical weight of a number of molecular energy levels, as a function of their energy above the ground state. In local thermodynamic equilibrium (LTE), this will just be a Boltzmann distribution, so a plot of the natural logarithm of N_u/g_u versus E_u/k will yield a straight line with a slope of $1/T$, where g_u is the statistical weight of the level u and E_u is its energy above the ground state. The temperature inferred is often called the “rotational temperature,” although it is not a priori restricted to a set of rotational energy levels. The temperature obtained would be expected to be equal to the kinetic temperatures if all levels were thermalized.

Linke, Frerking, & Thaddeus (1979) were among the first to apply this approach to determine the kinetic temperature in Sgr B2 using six rotational lines of CH_3SH (methyl mercaptan). They fit a linear function to their plot of log intensity versus energy to derive a rotational temperature of 9 K, considerably lower than estimates of the kinetic temperature using tracers such as ^{12}CO . A similar result, $T = 14$ K, was derived by Frerking, Linke, & Thaddeus (1979) using the linear molecule HNCS (isothiocyanic acid). It is difficult to understand how a hot region such as Sgr B2 could have such a low kinetic temperature unless these species trace a particularly cold subcondensation. A very extensive application of this approach was made much later by Turner (1991) using 36 species (including over 700 lines)

in Sgr B2 and 27 species (responsible for over 800 lines) in Orion KL. Turner noted problems with using some of this data, as the assumption of optically thin emission appears to break down. Turner fit most of the rotational diagrams with a single straight line, although in a few cases the data fell into two categories and two separate fits were made. In almost all cases the data have a considerable scatter around the fit, and in many (if not most) cases it is not clear that a single or even a piecewise linear fit is satisfactory. The rotational temperatures he found range from 9 K to over 200 K in Sgr B2 and 12 K to 120 K in OMC 1.

The rotation diagram approach was also used by Sutton et al. (1995) to derive the kinetic temperature in their study of the distribution of molecules in the core of OMC 1. These authors found that the molecular excitation can be reasonably well described by rotational temperatures 15–45 K for the extended ridge, 50–180 K for the hot core, and 50–130 K for the compact ridge and the plateau. A similar approach was taken by Serabyn & Weisstein (1995) to derive temperatures in the OMC core. Nummelin et al. (1998) analyzed emission from $c\text{-C}_2\text{H}_4\text{OH}$ (ethylene oxide), CH_3CHO (acetaldehyde), HCOOH (formic acid), CH_3OH (methanol), CH_5OH (ethanol), and CH_3OCH_3 (dimethyl ether) in five “hot core” sources. While some species in a given source (e.g., $c\text{-C}_2\text{H}_4\text{OH}$ and CH_3CHO) were found to have similar rotational temperatures, CH_3OCH_3 appears the most distinctly different, characterized by a much higher temperature. Thus, the rotation diagram can give important clues to chemical structure of these regions, but it is important to understand the uncertainties that are present.

In addition to hot star-forming cores there are many other structural and morphological features associated with the star formation process, including cold dark cores, molecular outflows, jets, disks, and ultracompact H II regions. It is important to determine the kinetic temperatures within all of these features to study the energetics and interactions in star-forming regions. For example Cesaroni et al. (1997) have attempted to derive the kinetic temperature for the disk outflow region of the high-mass protostar IRAS 20126+4104 using a rotation diagram. They observed emission from many levels of CH_3CN (methyl cyanide) and CH_3OH and derived temperatures of ≈ 50 K for the bulk of the gas and 150–260 K for the core. However, the data show a great deal of scatter and are far from linear over a wide range of excitation energy. In all of these studies, the total column density of each species has associated with it an uncertainty that is closely tied to the assumption of complete thermalization and the value of the inferred kinetic temperature. An additional error arises if the emission is not optically thin. To first order, the finite opacity produces an underestimate in the upper level column density of the observed transition, but it can also produce a more insidious error in the rotational temperature that is determined (which again impacts the total column density of the species in question).

The issue of finite optical depth in connection with the rotation diagram method has been discussed by Turner (1991) and by Olmi, Cesaroni, & Walmsley (1996), while Loren & Mundy (1984) and Olmi, Cesaroni, & Walmsley (1993) have considered the effects of non-LTE excitation on CH_3CN . Askne et al. (1984) and Bergin et al. (1994) have analyzed the excitation of CH_3CCH . In this paper we examine from a more general perspective, the conditions

and assumptions used to derive column densities, rotational temperatures, and thus the kinetic temperature, using what we prefer to call the “population diagram” method. We feel that this correctly reflects the idea of analyzing the populations of the various levels in a direct, graphical way. There are many situations in which the assumption of optically thin lines may not hold. The observer in general is unaware whether the lines observed appear optically thin because their opacity is truly small or because the emission is beam diluted (as could result from a highly clumped structure, for example). If a number of observed transitions do make a straight line in a population diagram where the logarithm of the integrated intensity per statistical weight is plotted against E_u , general practice has been to conclude that all levels are thermalized and that the excitation temperature is equal to the kinetic temperature. This important assumption also deserves investigation.

In § 2 of this paper we review the relationship between line emission and the observed antenna temperature and discuss various limiting cases. In § 3 we investigate how the integrated intensity, the upper level column density, and the total molecular column density are related in various situations. In § 4 we discuss the population diagram and the effects of finite optical depth when level populations are in LTE. We treat the case of linear molecules in some detail as analytic expressions are straightforward to obtain and use methanol as an example of a more complex molecular species. In § 5 we consider non-LTE excitation for both linear and more complex molecules and discuss effects on the population diagram. In § 6 we discuss some uses of the population diagram and indicate some of the advantages it offers for determination of the hydrogen density from multi-transition observations of molecular clouds.

2. LINE EMISSION AND ANTENNA TEMPERATURE

2.1. General Relationships

The antenna temperature T_a produced at a frequency ν by a source having brightness distribution $B_\nu(\theta, \phi)$ is given by (see, e.g., Kraus 1982, p. 99)

$$T_a = (A_e/2k) \int_{4\pi} B_\nu(\theta, \phi) P_n(\theta, \phi) d\Omega, \quad (1)$$

where $P_n(\theta, \phi)$ is the normalized power pattern of the antenna. This function describes the relative response of the antenna to signals coming from different directions, normalized such that on boresight, the direction of maximum response, $P_n(0, 0) = 1$, and $\int_{4\pi} P_n(\theta, \phi) d\Omega = \Delta\Omega_a$, the antenna solid angle. The integral in equation (1) can be conveniently expressed in terms of a source-antenna coupling factor if the source and antenna power pattern have some symmetry or other simplifying properties. Two limiting cases illustrate the behavior of equation (1): a point source and uniform emission filling the antenna beam.

Taking the solid angle subtended by a “pointlike” source to be much smaller than $\Delta\Omega_a$, we can take P_n to be equal to unity over the solid angle of the source. Further, if the source is uniform, B_ν can be removed from the integral, which is then the source solid angle $\Delta\Omega_s$. In this situation we can write

$$T_a = (A_e/2k)(\Delta\Omega_a) \left(\frac{\Delta\Omega_s}{\Delta\Omega_a} \right) B_\nu, \quad (2)$$

where the expression in the third parentheses is the beam dilution factor.

From the “antenna theorem” (Kraus 1982, p. 157), $A_e \Delta\Omega_a = \lambda^2$, so we can rewrite equation (2) as

$$T_a = (\lambda^2/2k) \left(\frac{\Delta\Omega_s}{\Delta\Omega_a} \right) B_v. \quad (3)$$

If an extended source is uniform over the antenna solid angle, we can take B_v out of the integral in equation (1), which then becomes $\Delta\Omega_a$. The antenna theorem then gives us $T_a = (\lambda^2/2k) B_v$. The beam dilution factor is thus much less than unity for very small sources, and reaches a maximum value of unity for an extended, uniform source.

The brightness produced by a source at temperature T having optical depth τ is

$$B_v = \frac{h\nu/k}{e^{h\nu/kT} - 1} (1 - e^{-\tau}). \quad (4)$$

However, for reasons that will become clear momentarily, it is convenient to write this as

$$B_v = \frac{h\nu/k}{e^{h\nu/kT} - 1} \left(\frac{1 - e^{-\tau}}{\tau} \right) \tau. \quad (5)$$

We can write the optical depth of the transition as

$$\tau = \frac{h}{\Delta v} N_u B_{ul} (e^{h\nu/kT} - 1), \quad (6)$$

where N_u is the column density in the upper state, B_{ul} is the Einstein B -coefficient for the transition, and Δv is the full width at half-maximum line width in units of velocity. (More exactly, we should employ the line profile function evaluated at the peak of the line, but this is very close to $1/\Delta v$ for a Gaussian or similar line profile.)

Substituting equations (6) and (5) into equation (3), together with the relationship that $B_{ul} = A_{ul} c^3 / 8\pi h \nu^3$, we obtain

$$T_a = \frac{hc^3 N_u A_{ul}}{8\pi k \nu^2 \Delta v} \left(\frac{\Delta\Omega_s}{\Delta\Omega_a} \right) \left(\frac{1 - e^{-\tau}}{\tau} \right). \quad (7)$$

Note that this expression does not explicitly include the temperature of the source.

We can invert equation (7) to yield an expression for the upper level column density in terms of the observed quantity, T_a . It is often convenient to consider the integrated line intensity,

$$W = \int T_a dv, \quad (8)$$

which in our usage is just $T_a \Delta v$, to obtain

$$N_u = \frac{8\pi k \nu^2 W}{hc^3 A_{ul}} \left(\frac{\Delta\Omega_a}{\Delta\Omega_s} \right) \left(\frac{\tau}{1 - e^{-\tau}} \right). \quad (9)$$

2.2. Limiting Cases

Different analysis techniques, including population and rotation diagram analysis, have as inputs the upper level column density. It is a considerable simplification to make

the two assumptions that (1) the source fills the beam and (2) the emission is optically thin. If these are both satisfied, each of the two expressions in parentheses in equation (9) is equal to unity, and we obtain the relationship

$$N_u^{\text{thin}} = \frac{8\pi k \nu^2 W}{hc^3 A_{ul}}, \quad (10)$$

which can often be found in the literature. We define γ_u as the combination of constants relating the integrated intensity and the upper level column density in this limit. Thus we have

$$\gamma_u = \frac{8\pi k \nu^2}{hc^3 A_{ul}} \quad (11)$$

and

$$N_u^{\text{thin}} = \gamma_u W. \quad (12)$$

This useful result can also be obtained starting with the basic definition of brightness of an optically thin source, ignoring any background radiation,

$$B_v = \frac{A_{ul} N_u^{\text{thin}} h\nu}{4\pi \Delta v} = \frac{A_{ul} N_u^{\text{thin}} hc}{4\pi \Delta v}. \quad (13)$$

This yields

$$T_a = \frac{hc^3 A_{ul} N_u^{\text{thin}}}{8\pi k \nu^2 \Delta v}, \quad (14)$$

or

$$W = \frac{A_{ul} hc^3 N_u^{\text{thin}}}{8\pi k \nu^2} = \frac{N_u^{\text{thin}}}{\gamma_u}, \quad (15)$$

which is just the inverse of equation (12).

If the first assumption is not valid and the source does not fill the beam, then the correct upper level column density is greater than that obtained assuming the beam to be filled by a factor equal to $\Delta\Omega_a/\Delta\Omega_s$. This correction can be substantial but can be tested definitively only by observing with higher angular resolution. In this section, we will assume that the source uniformly fills the antenna beam and return to the issue of a nonuniformly filled beam in § 6.2.

We now consider possibly optically thick emission, but, since we are assuming that the source does fill the antenna beam, we set $\Delta\Omega_a/\Delta\Omega_s = 1$ in equation (9). We define the optical depth correction factor C_τ ,

$$C_\tau = \frac{\tau}{1 - e^{-\tau}}, \quad (16)$$

and we find that

$$N_u = \gamma_u W C_\tau = N_u^{\text{thin}} C_\tau. \quad (17)$$

The optical depth correction factor defined here is greater than or equal to unity. It is the factor by which the upper level column density derived from observed integrated intensity W would appear to be too small as a result of the finite optical depth. Hence, to obtain the correct value of N_u , we must multiply N_u^{thin} by C_τ as indicated in equation (17).

Direct determination of the optical depth by comparison with emission from other isotopomers, measurement of hyperfine ratios, or other means, is rarely straightforward. We will show below, how the “population diagram” can also be used as a diagnostic of the optical depth of the emission.

3. RELATING UPPER LEVEL AND TOTAL COLUMN DENSITIES

To understand different possible behavior in the “population diagram,” we need to be able to calculate W for each level and then see what value of N_u is found and how it depends on the energy of the transition, as well as on other factors.

3.1. Non-LTE Excitation

In the case of arbitrary excitation, a different temperature may characterize the population of each level relative to that of the ground state or relative to that of any other level. The excitation temperature T_{ex} is defined by the relative populations or column densities of any two levels i and j of statistical weights g_i and g_j and energies E_i and E_j relative to an arbitrary common reference, through

$$\frac{N_j}{N_i} = \frac{g_j}{g_i} \exp [-(E_j - E_i)/kT_{\text{ex}}] . \quad (18)$$

The excitation temperature can be defined whether or not the two levels in question are connected by a radiative transition, although it is only in this situation that T_{ex} can be directly measured.

3.2. LTE

For a molecule in local thermodynamic equilibrium (LTE), all excitation temperatures are the same, and taking this to be given by T , the population of each level is given by

$$N_u = \frac{N}{Z} g_u e^{-E_u/kT} , \quad (19)$$

where N is the total column density of the species in question, and Z is the partition function, given by

$$Z = \sum_{\text{all levels}} N_i . \quad (20)$$

In LTE it is straightforward to obtain the total molecular column density from the column density of any individual transition if T is known. If the molecule's transitions are not thermalized, the fractional population of a given level can be greater or less than that in LTE, so it is difficult to make a general statement about how the determination of the total column density is affected. We will return to this topic in § 5.

4. THE POPULATION DIAGRAM

A population diagram can be useful to assess whether the emission is optically thick or thin, to assess whether the level populations are described by LTE, and to determine what temperature describes the population distribution in the event that LTE applies.

4.1. Population Diagram and LTE

The “traditional” rotation diagram is based on the supposition that all level populations are described by LTE. We then rewrite equation (19) to obtain

$$\ln \frac{N_u}{g_u} = \ln N - \ln Z - \frac{E_u}{kT} . \quad (21)$$

We can also include the possibility of finite optical depth explicitly using equation (17):

$$\ln \frac{N_u^{\text{thin}}}{g_u} + \ln C_\tau = \ln N - \ln Z - \frac{E_u}{kT} . \quad (22)$$

If the optical depth is small, C_τ is unity, and from equation (17), $N_u = N_u^{\text{thin}}$. Thus, the logarithm of the upper level column density per statistical weight does show a linear dependence on upper level energy. This is directly translatable to an observational relationship through equation (10), giving us

$$\ln \frac{\gamma_u W}{g_u} = \ln N - \ln Z - \frac{E_u}{kT} . \quad (23)$$

If the optical depth is not small compared to unity, then we must use equation (22), which can be written in terms of the observed W as

$$\ln \frac{\gamma_u W}{g_u} = \ln N - \ln C_\tau - \ln Z - \frac{E_u}{kT} . \quad (24)$$

If we were not aware of the finite optical depth and thus took C_τ equal to 1, each of the upper level populations would be underestimated by a factor C_τ , which is different for each transition. The ordinate of the rotation diagram would consequently be below its correct value by an amount $\ln C_\tau = \ln [\tau/(1 - e^{-\tau})]$.

4.2. Optical Depth for Rotational Transitions of Linear Molecules

For a linear molecule we can label each state by its rotational quantum number, J , its energy, $E_J = hB_0 J(J+1)$, and its statistical weight, $g_J = 2J+1$. The frequency of the transition $J \rightarrow J-1$ is given by $\nu_{J,J-1} = 2B_0 J$, and the corresponding Einstein A -coefficient is given by

$$A_{J,J-1} = \frac{64\pi^4 \nu^3 \mu^2}{3hc^3} \frac{J}{2J+1} , \quad (25)$$

where μ is the permanent electric dipole moment. The Einstein B -coefficient is

$$B_{J,J-1} = \frac{8\pi^3 \mu^2}{3h^2} \frac{J}{2J+1} . \quad (26)$$

We can write the optical depth of the transition $J \rightarrow J-1$ as

$$\tau_{J,J-1} = \frac{8\pi^3 \mu^2}{3h} \frac{N}{\Delta \nu} \frac{1}{Z} J e^{-aJ(J+1)} (e^{2aJ} - 1) , \quad (27)$$

where we have defined

$$a = hB_0/kT . \quad (28)$$

4.3. Linear Molecules in LTE

If LTE applies, and we are in a relatively warm cloud so that $kT > hB_0$, we can make the substitution $u = J(J+1)$ and transform the partition function into an integral:

$$Z = \sum_{J=0}^{\infty} (2J+1) e^{-hB_0 J(J+1)/kT} \rightarrow \int_0^{\infty} e^{-au} du. \quad (29)$$

This yields the simple result that $Z = a^{-1} = kT/hB_0$, which is surprisingly accurate even for temperatures as low as $T \sim B_0/2k$.

The variation of τ as a function of energy and J for a linear molecule in LTE is given by equation (27) with $Z = a^{-1}$. It is shown in Figure 1, which gives the relative values of the optical depths of the different transitions as a function of J of the upper level.

For $a < 1$, the optical depth exhibits a peak at a value of J that we take to be equal to $J_{\max\tau}$. If we are in the limit $aJ_{\max} < 1$, the value of $J_{\max\tau}$ is given by

$$J_{\max\tau} = 1/\sqrt{a} = \sqrt{kT/hB_0}. \quad (30)$$

The energy of the transition having maximum optical depth is just $E_{\max\tau} = hB_0 J_{\max\tau}(J_{\max\tau} + 1)$, and, for $J_{\max\tau} \gg 1$, we find the plausible result that

$$E_{\max\tau} = kT. \quad (31)$$

The frequency of the transition of maximum opacity is then

$$\nu_{\max\tau} = 2B_0 J_{\max\tau} = 2B_0/\sqrt{a}. \quad (32)$$

A convenient conversion factor is

$$a = 0.048 B_0(\text{GHz})/T(\text{K}), \quad (33)$$

so that

$$J_{\max\tau} = 4.6 \sqrt{T(\text{K})/B_0(\text{GHz})} \quad (34)$$

and

$$\nu_{\max\tau}(\text{GHz}) = 9.13 \sqrt{T(\text{K})B_0(\text{GHz})}. \quad (35)$$

These expressions give an idea of which transition, at what frequency, will suffer the most from the effect of optical depth. For example, for HC_3N having $B_0 \simeq 4.6$ GHz, for $T = 10$ K, $J_{\max\tau} = 7$ and $\nu_{\max\tau} = 61$ GHz. This suggests that, for somewhat warmer clouds, the $\lambda \simeq 3$ mm transitions of this molecular species will be the most affected by optical depth effects.

4.4. Effect of Optical Depth and The Optical Depth Correction Factor for Linear Molecules Having Finite Values of τ

In Figure 2 we present population diagrams calculated for the molecule HC_3N , which has rotation constant $B_0 = 4.55$ GHz and permanent electric dipole moment $\mu = 3.72$ D (Lafferty & Lovas (1978)). For the example shown with $T_K = 22$ K, $a = hB_0/kT = 0.01$, and a hydrogen density of 10^9 cm^{-3} is sufficient to thermalize all of the transitions with significant population. These calculations were carried out using a large velocity gradient radiative-transfer code, for which, in addition to the hydrogen density and kinetic temperature, the input needed is the fractional abundance per velocity gradient of the species being studied. This

quantity, when multiplied by the hydrogen density, is equal to the column density of the species in question per unit line width, which determines the optical depth in any model. A velocity gradient of $1 \text{ km s}^{-1} \text{ pc}^{-1}$ or line width equal to 1 km s^{-1} and size equal to 1 pc are typical for molecular clouds, and in this case the fractional abundance per unit line width is numerically equal to the fractional abundance itself. We shall in the following refer to fractional abundances rather than fractional abundances per unit line width, when there is no danger of confusion, and adopt a line width of 1 km s^{-1} where a specific value is required.

For the lowest value of the fractional abundance, 10^{-15} , we do indeed see a linear curve as expected from optically thin emission from a molecule in LTE. When the fractional abundance is increased by a factor of 10, the curve has moved up by close to this factor and is still nearly linear. As the fractional abundance increases further, the curves become highly nonlinear and lie well below the values that would be extrapolated from the optically thin results. The divergence from linear behavior is most striking for transitions with $3 \leq J_u \leq 12$, which is the range for which the optical depths are largest.

Once a particular transition has become optically thick, the value of $\gamma_u W/g_u$ cannot increase further, and in comparing the results for the two largest fractional abundances, we see that there is a small change only for the $J = 1 \rightarrow 0$ transition, which has the lowest optical depth of all those considered. Thus, changing the HC_3N fractional abundance from 10^{-12} to 10^{-11} has essentially no effect, as all transitions are already optically thick for the lower value.

The limiting form of the population diagram when all transitions are optically thick is determined by the fact that the antenna temperature is that produced by a blackbody. In the Rayleigh-Jeans limit, this yields (with a defined in eq. [28])

$$\frac{\gamma W}{g_u} = \frac{2\Delta\nu}{16\pi^3\mu^2} \frac{1}{aJ^2}, \quad (36)$$

where $\Delta\nu$ is the line width. The nonlinear behavior on the semi-log plot can have several different effects, which appear even in the cases of moderate fractional abundance when all transitions except for the lowest and highest are optically thick. From Figure 2, with incomplete and necessarily imperfect data, it would be possible to conclude that two different temperature components were present, while in fact one is seeing the effect of the finite opacity. For example, with $X = 10^{-13}$, if one fits the five lowest transitions, one obtains an anomalously low temperature of 6.5 K, while using the five highest transitions included in Figure 2, one obtains the erroneously high value of 51 K (compared to the actual value of 22 K). This effect is even more extreme for higher optical depths, and while the predicted intensities for lower values of J are less linear, it would be possible to think, if one were not aware of the large values of the optical depth, that a fraction of the gas were thermalized at a very low temperature. For very high values of J , the level populations drop and the transitions become optically thin, which results in these points falling on a line consistent with the correct temperature.

If not properly accounted for, the finite optical depth results in an underestimate of the total molecular column density. The situation is complicated by the fact that a linear fit would evidently not be satisfactory for the full

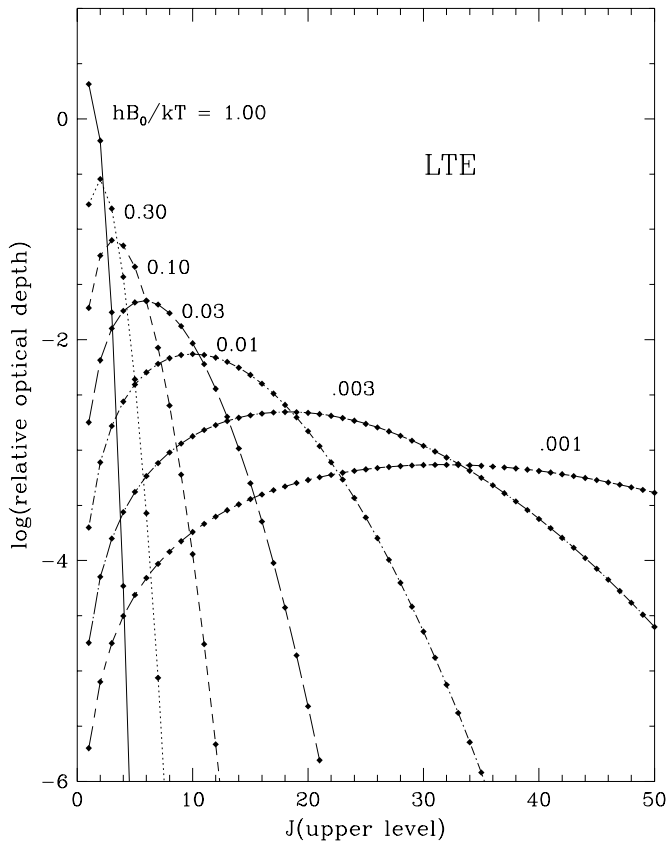


FIG. 1.—Variation of relative optical depth of rigid rotor transitions in LTE as a function of J for different values of the rotation constant relative to the kinetic temperature.

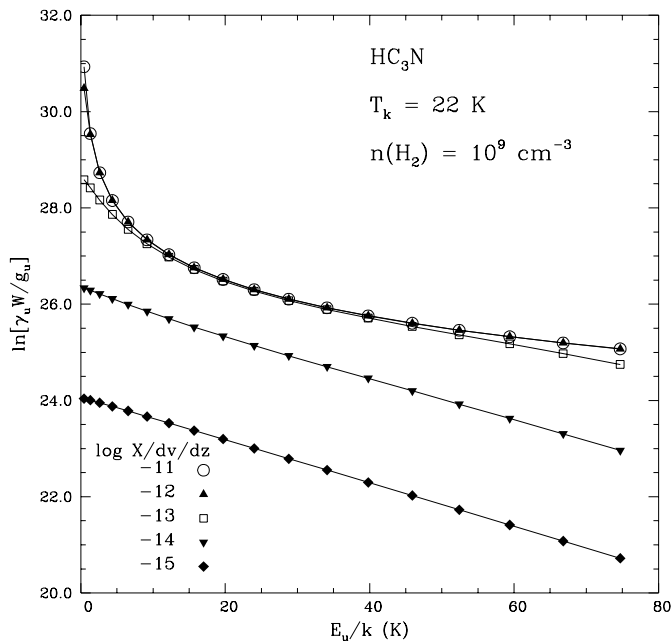


FIG. 2.—Population diagrams for HC_3N . The H_2 density of 10^9 cm^{-3} ensures that all transitions are thermalized, so that LTE applies. At the kinetic temperature of 22 K, $a = hB_0/kT = 0.01$. The curves correspond to different fractional abundances per unit velocity gradient as indicated by the symbols shown in the lower left. The maximum optical depth for $X = 10^{-11}$ is 377, which occurs for the $J = 10 \rightarrow 9$ transition. The corresponding optical depth of the $1 \rightarrow 0$ transition is 10, and for the $18 \rightarrow 17$ transition is 130. The optical depths scale directly with the fractional abundance.

range of transitions included in Figure 2. If we ignore the finite optical depth, we would use equation (21), which gives that the value of the ordinate extrapolated to zero upper state energy is equal to N/Z . The different temperatures that one would derive from straight lines fit to the different sections of the curve also enter through the fact that the partition function is proportional to the temperature derived. For a fractional abundance per unit velocity gradient of $10^{-13} (\text{km s}^{-1} \text{ pc}^{-1})^{-1}$ and a line width of 1 km s^{-1} , the total HC_3N column density is $3.08 \times 10^{14} \text{ cm}^{-2}$. Using only the data from the lower J transitions, we find $\ln(N/Z)$ equal to 28.7, and with the derived temperature of 6.5 K, we obtain $N = 9 \times 10^{13} \text{ cm}^{-2}$. For the highest five transitions, we obtain, with the derived temperature of 51 K, $N = 1 \times 10^{14} \text{ cm}^{-2}$.

In both of these cases we have assumed that all levels are characterized by the parameters derived from the limited range of J . The lower transitions give an intercept that is not far from the value extrapolated from optically thin results, but the erroneously low temperature results in a column density that is too low by almost a factor of 3.5. If the higher J transitions are used, the intercept is dominated by these very optically thick lines, and the erroneously high temperature only partially compensates, with the final result being too low by approximately a factor of 3. The maximum value of τ in this example is 3.8, and from equations (16) and (17) we would anticipate an underestimate of the upper state column densities in the middle J range of approximately this factor. We see that since these levels are those that do have a large fraction of the total molecular population, the total column density is underestimated by a factor only slightly less than the peak optical depth.

In Figure 3 we show more generally the effect of omitting the optical depth correction factor, in terms of how it would affect the left-hand side of a rotation diagram such as that indicated in equation (24). If we ignored the finite optical depth issue, the observationally determined integrated intensities directly give the upper level column densities, which would exhibit a Boltzmann distribution, characterized by a straight line on a semi-log plot. We have plotted the negative of the natural logarithm of the optical depth correction factor so that the appearance of the curves mimics the effect on the relationship in a population diagram.

Figure 3 shows C_τ for three different values of hB_0/kT , which is equal to 0.001 in Figure 3a, 0.01 in Figure 3b, and 0.1 in Figure 3c. The energy of the transition having the maximum optical depth is always given by equation (31). We see that the form of the variation of C_τ as a function of optical depth is essentially independent of E_u/kT but that the quantitative behavior does depend on this parameter. For fixed molecular parameters and column density, the maximum value of τ varies as a (in the limit $a < 1$). However, the optical depth of the $J = 1$ to $J = 0$ transition varies as a^2/e in this same limit, so that the ratio of the optical depth of the most optically thick transition to that of the $J = 1$ to 0 transition is

$$\frac{\tau_{\max}}{\tau_{1,0}} = \frac{1}{ea}, \quad (37)$$

again in the limit $a < 1$. This result is confirmed by numerical calculations to be quite accurate for a as small as 0.1. For a given value of $\tau_{1,0}$, as $a (= hB_0/kT)$ increases, the level

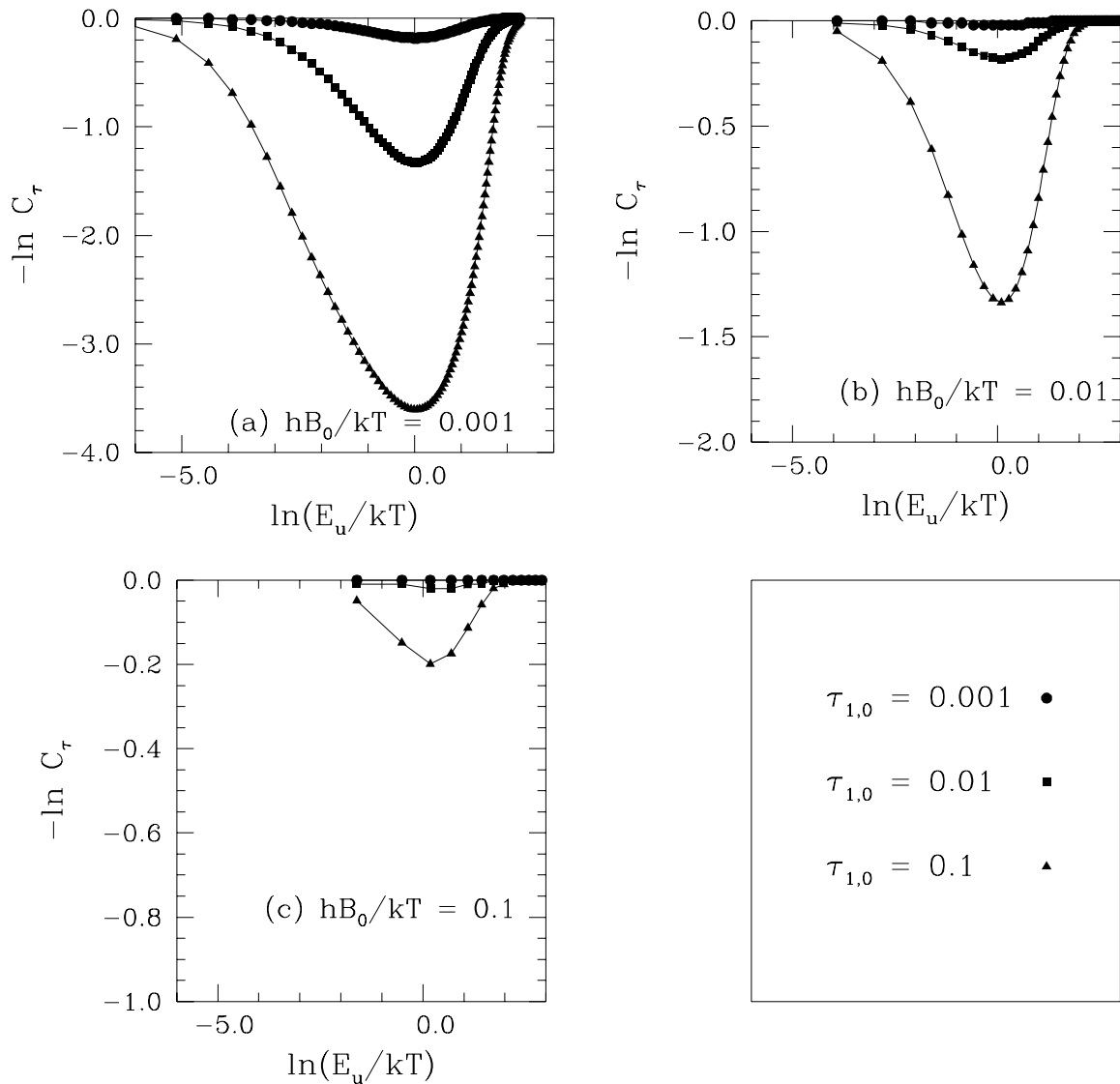


FIG. 3.—Optical depth correction factor as a function of upper level energy for different values of the opacity of the $\text{HC}_3\text{N } 1 \rightarrow 0$ transition. The value of $a = hB_0/kT$ is indicated in each panel. The circles are for $\tau_{1,0} = 0.001$, the squares for $\tau_{1,0} = 0.01$, and the triangles for $\tau_{1,0} = 0.1$. The negative of the natural logarithm of C_τ is plotted so that the resulting curves have the same orientation as the effect of the finite optical depth on the population diagram.

having maximum τ decreases, as does the maximum value of τ . Hence, for the same value of $\tau_{1,0}$, the correction factors seen in Figures 3b and 3c are closer to unity than those in Figure 3a.

4.5. Nonlinear Molecules in LTE

A wide variety of molecules have been detected in interstellar clouds, with many having more complex energy-level structures than the simple linear molecules discussed above. In general, there can be several transitions from a given state, and the dependence of transition frequencies on the energy of the upper state is more complex.

Here we give some results for the E species of CH_3OH , a molecule that has relatively large abundances in dense clouds and has been found to have an enhanced abundance in molecular outflows. The energy levels, labeled “J” and “K,” are shown in Figure 4, along with representative transitions, which obey the selection rules $\Delta J, \Delta K = 0, \pm 1$.

However, because of the asymmetry in the energy levels with respect to the sign of K, “ladders” having different values of K have quite different arrangements of allowed transitions. In particular, states with $K = 3$ and $K = -3$ (excepting the lowest ones) have (in addition to a transition with $\Delta K = 0$) two strong downward transitions with relatively large frequencies, resulting in total spontaneous decay rates between 10^{-3} s^{-1} and 10^{-2} s^{-1} for the levels considered here. The $K = -1$ levels have, in contrast, only two downward transitions with relatively modest frequencies, and total spontaneous decay rates that do not exceed a few times 10^{-4} s^{-1} . The situation for the other K ladders is intermediate. As a result, the H_2 densities required to thermalize the level populations vary over a considerable range, from $\simeq 10^8 \text{ cm}^{-3}$ for $K = \pm 3$ levels to $\simeq 10^6 \text{ cm}^{-3}$ for the $K = -1$ ladder. The different transitions also have very different absorption coefficients, so that their optical depths vary considerably for a given molecular abundance. With

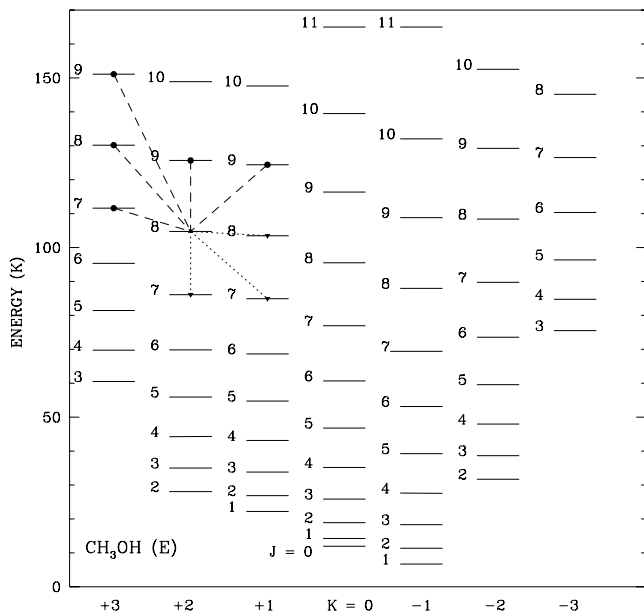


FIG. 4.—Energy levels below $E/k = 160$ K with $|K| \leq 3$ for E-type methanol with quantum numbers J and K indicated. We show the radiative transitions that involve the (8, 2) level. There are five transitions into this level (dashed lines); three with $\Delta K = +1$, one with $\Delta K = 0$, and one with $\Delta K = -1$. There are three transitions out of the (8, 2) level (dotted lines), one with $\Delta K = 0$, and two having $\Delta K = +1$.

the collision rate coefficients adopted here (discussed in § 5.3), hydrogen densities greater than 10^9 cm^{-3} are required to bring all of the transitions considered here into LTE. Population diagrams for $n(\text{H}_2) = 10^9 \text{ cm}^{-3}$ as a function of fractional abundances of CH_3OH are shown in Figure 5. As for the previous example, we adopt a velocity gradient of $1 \text{ km s}^{-1} \text{ pc}^{-1}$ and a line width of 1 km s^{-1} , and refer to the fractional abundances, which are numerically equal to the fractional abundances per unit velocity gradient. For the lowest abundance considered, $X(\text{CH}_3\text{OH}) = 10^{-14}$, all transitions are optically thin and we obtain a straight line corresponding to the kinetic temperature of 50 K. Note that, since all opacities are $\ll 1$, the various transitions with a common upper level all appear as a single point on the straight line. As the fractional abundance increases, the transitions with greater absorption coefficients become optically thick, and, for $X(\text{CH}_3\text{OH}) = 10^{-12}$, we see that a number of transitions have upper level populations significantly below those extrapolated from optically thin results. For $X(\text{CH}_3\text{OH}) = 10^{-11}$ we see a greatly enhanced apparent “scatter” in the population diagram, since some transitions have clearly reached their optically thick limiting value, while others, defining the upper edge of the envelope, are still close to being optically thin.

For a species with complex energy level structure such as CH_3OH , it is difficult to draw simple, general conclusions about the effect of finite τ , as is possible for linear molecules. Our modeling suggests that optically thick emission even in LTE can significantly increase the scatter in the data if a mixture of thin and thick transitions are included. Given that the transitions we consider cover frequencies between 6.9 and 633 GHz, actual data sets may not only exhibit an increased scatter but could also indicate erroneous temperatures and column densities, depending on which particular transitions are included. Thus, the potential deleterious

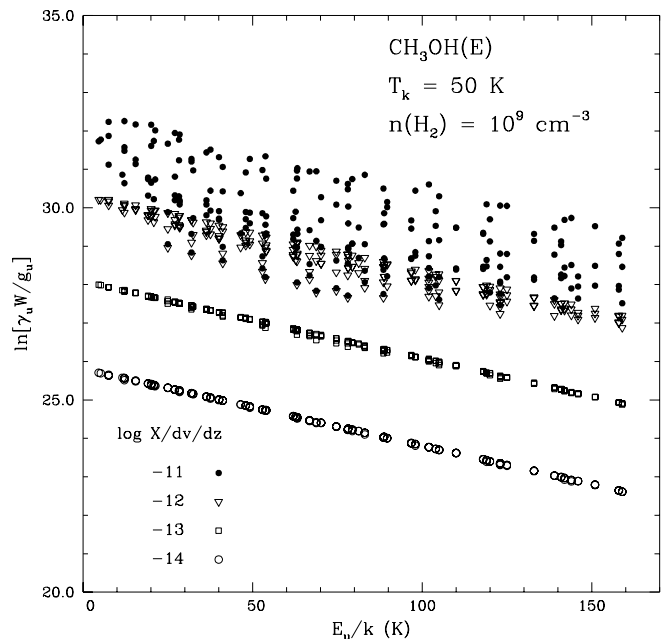


FIG. 5.—Population diagrams for E-type methanol based on levels below $E/k = 160$ K having $|K| \leq 3$. We take a velocity gradient equal to $1 \text{ km s}^{-1} \text{ pc}^{-1}$, so that the fractional abundances per unit velocity gradient indicated in the lower left correspond to the fractional abundances of CH_3OH . For the lower CH_3OH fractional abundances, there are generally more than one optically thin transition from a given upper level, which all appear as a single point. As the fractional abundance increases, the transitions with larger optical depth fall below those extrapolated from optically thin results. For $X(\text{CH}_3\text{OH}) = 10^{-11}$, there are transitions with τ as low as 0.25, and as large as 30, which produces the apparent scatter in the upper level column densities derived without correction for the finite optical depths.

effect of uncorrected optical depths cannot be ignored for more complex molecules.

5. NON-LTE EXCITATION

We next examine what happens if the hydrogen density is insufficient to thermalize some or all of the transitions, so that the populations of the energy levels used in forming the population diagram cannot be described by LTE. We restrict ourselves again only to the cases of HC_3N as representative of linear molecules and CH_3OH as an example of more complex molecular species.

5.1. Linear Molecules

For the calculations described in this section we have used the collision rate coefficients of Green & Chapman (1978), which include the lowest 24 levels of HC_3N . We have not explicitly included a correction for H_2 rather than He as the collision partner, which would reduce the actual density corresponding to each density given by approximately 50%. In Figure 6 we show results for densities between 10^3 and 10^8 cm^{-3} . The fractional abundance of HC_3N per unit velocity gradient is $10^{-15} (\text{km s}^{-1} \text{ pc}^{-1})^{-1}$, which results in all transitions being optically thin for all H_2 densities. For densities $\geq 10^6 \text{ cm}^{-3}$, the populations of the levels considered here are thermalized, so that the population diagrams are essentially straight lines corresponding to the kinetic temperature of 22 K.

The behavior for lower densities is more surprising, however. While none of these curves forms a perfect straight line as do the ones for higher densities, for a significant range of energies (excepting the lowest transitions), each can

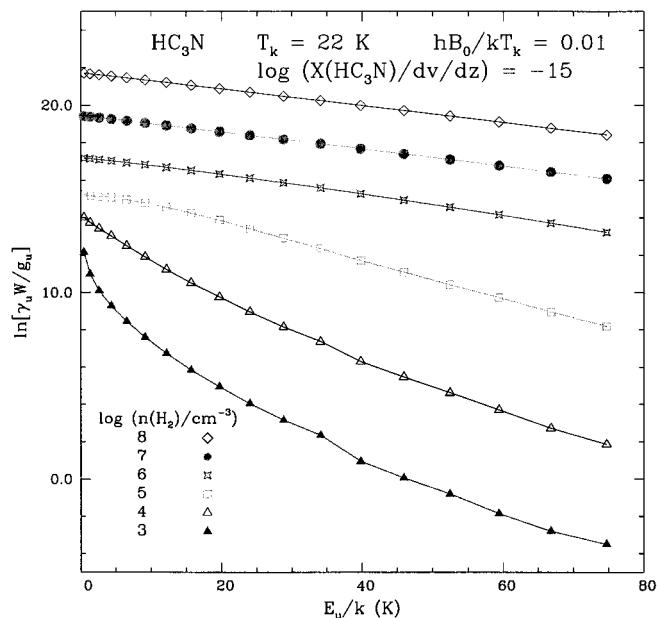


FIG. 6.—Population diagrams for HC_3N levels up to 70 K above the ground state (including $J = 0$ to $J = 18$). The fractional abundance of HC_3N per unit velocity gradient is chosen to make all transitions optically thin for all hydrogen densities considered, which vary from 10^3 cm^{-3} to 10^8 cm^{-3} as indicated by the symbols shown at lower left of figure. For hydrogen densities $n(\text{H}_2) \geq 10^7 \text{ cm}^{-3}$, all transitions are thermalized and the population diagram curves are straight lines characteristic of the kinetic temperature of 22 K. For lower densities, a variety of effects are seen, including quasi thermalization at a temperature considerably less than the kinetic temperature.

be fit satisfactorily with a straight line. The temperatures implied are 6 K for $n(\text{H}_2) = 10^3 \text{ cm}^{-3}$, 7 K for $n(\text{H}_2) = 10^4 \text{ cm}^{-3}$, and 8 K for $n(\text{H}_2) = 10^5 \text{ cm}^{-3}$. All of these are decisively subthermal, and yet it would be difficult to recognize this unless we had data that included the transitions for $J \leq 6$ and $J > 20$. However, the latter would be relatively weak under these conditions, and thus difficult, or impossible, to observe.

The results seen here are unexpected because the range of spontaneous decay rates for the levels considered here is very large. From equation (25) we find that $A_{1,0} = 4 \times 10^{-8} \text{ s}^{-1}$, $A_{6,5} = 1.1 \times 10^{-5} \text{ s}^{-1}$, and $A_{20,19} = 4 \times 10^{-4} \text{ s}^{-1}$. Thus, the transitions that have an excitation temperature considerably less than the kinetic temperature include a range in spontaneous decay rates of approximately 50. Naively, one might expect that, since the transitions are neither totally unexcited nor thermalized, those with higher spontaneous decay rates would have lower excitation temperatures, as the collisional rates are essentially independent of the rotational quantum number of the initial state.

The quite different behavior that we find is a result of the manner in which the A -coefficients, transition frequencies, and collisional rate coefficients depend on J . For linear molecules, a general result is that the excitation temperature is not a monotonically decreasing function of J , despite the fact that the A -coefficients vary as J^3 . Rather, T_{ex} can be largely independent of J or even increase with increasing J , for conditions of relevance in interstellar clouds. This produces the “quasi-thermal” linear curves in Figure 6, with excitation temperatures much less than the kinetic temperature. Collisional cross sections that emphasize transitions in which J changes by several units enhance this

effect. The issue of the dependence of the excitation temperature on J is discussed further in the Appendix.

5.2. Non-LTE Excitation and Optical Depth Effects for Linear Molecules

We next consider non-LTE effects together with finite optical depths. The combination is significant because the absorption coefficients for the lower J transitions become larger when the hydrogen density is low, and the molecular population is concentrated in these levels. As shown in Figure 7, the effect is largely what one might expect from the combination of the two separate factors.

At the lower density modeled here, $n(\text{H}_2) = 10^4 \text{ cm}^{-3}$, the greatest optical depth occurs for $5 \leq J_u \leq 9$, so these transitions are the first to deviate from the quasi-thermal excitation curve as the fractional abundance of HC_3N is increased. There is a range of HC_3N fractional abundances per unit velocity gradient, starting at $X(\text{HC}_3\text{N})/dv/dz = 10^{-7} (\text{km s}^{-1} \text{ pc}^{-1})^{-1}$, in which the slope of the excitation curve, in the range of transitions lying somewhat above those having maximum optical depth, is increased by the radiative trapping. Thus, the excitation temperature that would be derived from these transitions is enhanced by the trapping. This situation is restricted by the radiative thermalization that is produced when the optical depth reaches a sufficiently high value, with the excitation curve approaching the limiting form determined by black body emission, as discussed in § 4.4.

5.3. Nonlinear Molecules

Non-LTE excitation for nonlinear molecules is more complex than for linear species. We again consider E-type methanol as a representative example. We have used the collisional rate coefficients of Peng & Whiteoak (1993), which are not rigorous calculations, but which should be satisfactory for our purpose. Our results do not demand

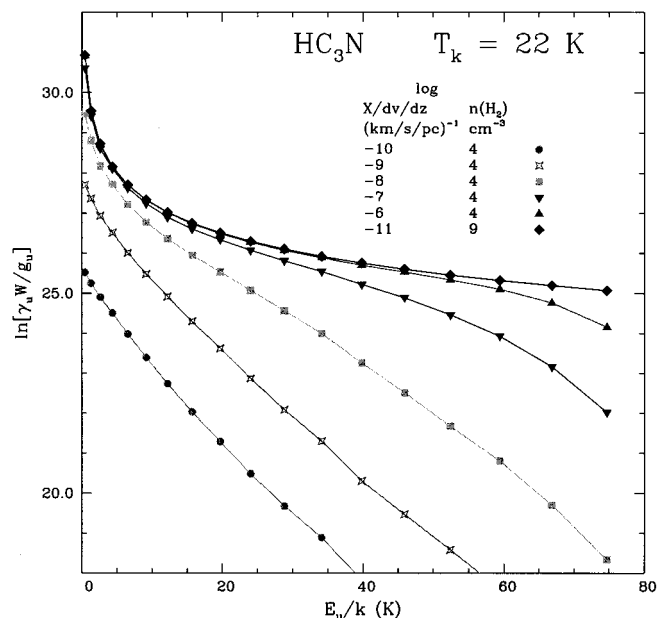


FIG. 7.—Effect of finite optical depth on subthermally excited HC_3N . The curves are for different molecular fractional abundances. A velocity gradient of $1 \text{ km s}^{-1} \text{ pc}^{-1}$ has been used to form the population diagrams. The integrated intensity is limited by the optically thick LTE curve (diamonds). The maximum values of the optical depth for collisional excitation alone are in the region $5 \leq J_u \leq 9$, while for LTE, the optical depth distribution is much more widely distributed and peaks at $J_u = 11$.

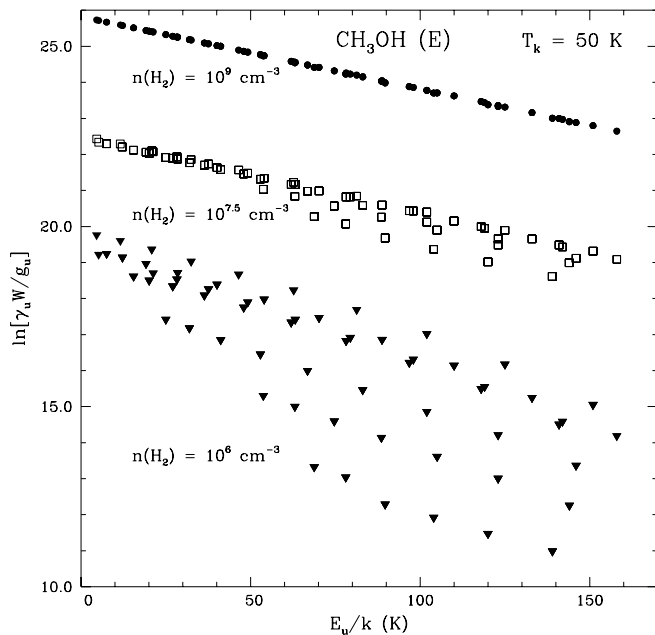


FIG. 8.—Population diagrams for optically thin CH_3OH at hydrogen densities of 10^6 , $10^{7.5}$, and 10^9 cm^{-3} . The fractional abundance per unit velocity gradient of CH_3OH is $10^{-14} (\text{km s}^{-1} \text{ pc}^{-1})^{-1}$ and a velocity gradient of $1 \text{ km s}^{-1} \text{ pc}^{-1}$ has been used to construct the population diagrams. For the lowest hydrogen density, the upper levels from different K ladders are relatively distinct, with the lowest group being the transitions in the $K = -3$ ladder, the next group the transitions in the $K = +3$ ladder, then those in the $K = -2$ ladder, while the highest group includes transitions in the remaining ladders. At a density of $10^{7.5} \text{ cm}^{-3}$, only the levels from the $K = -3$ ladder are significantly below the LTE curve, while for the highest H_2 density, all transitions considered here are essentially thermalized.

detailed modeling of the behavior of any single transition. Results for three hydrogen densities for which all transitions are optically thin are shown in Figure 8. The CH_3OH fractional abundance per unit velocity gradient is $10^{-14} (\text{km s}^{-1} \text{ pc}^{-1})^{-1}$, and we have used a line width of 1 km s^{-1} to form the population diagram. This is equivalent to $N(\text{CH}_3\text{OH})/\Delta v = 3.084 \times 10^4 n(\text{H}_2) \text{ cm}^{-2} (\text{km s}^{-1})^{-1}$.

For the lowest density, 10^6 cm^{-3} , we see a clear segregation of the points according to the K -ladder of the upper level of the transition. The lowest set of points corresponds to $K = -3$, the next to $K = +3$, and the next to $K = -2$. The transitions from states with $K = +2$, $+1$, and 0 comprise the cluster of points at somewhat higher values of integrated intensity, while the $K = -1$ transitions fall on a straight line just above this. This separation is due to the quite different densities required for thermalization, as discussed in § 4.5. The levels with different J for a given value of K all have the same excitation temperature at each hydrogen density, with $T_{\text{ex}} \simeq 31 \text{ K}$ for $n_{\text{H}_2} = 10^6 \text{ cm}^{-3}$, $T_{\text{ex}} \simeq 45 \text{ K}$ for $n_{\text{H}_2} = 10^{7.5} \text{ cm}^{-3}$, and $T_{\text{ex}} = T_k = 50 \text{ K}$ for $n_{\text{H}_2} = 10^9 \text{ cm}^{-3}$. The large scatter in the population diagram can thus be an indication of different degrees of subthermal excitation resulting from variations in the spontaneous decay rates. Again, however, a large range of transitions must be observed to determine the excitation temperature unambiguously.

6. DISCUSSION

In the preceding discussion, we demonstrated that a generalization of the traditional rotation diagram approach

improves the capability for analysis of multitransition data to determine excitation temperatures and molecular column densities. Careful consideration of the effects of optical depth and non-LTE excitation offer the possibility of improved accuracy, as well as understanding some of the apparently surprising behavior seen in various observational studies. Here we review and comment on some earlier work using the rotation diagram method, discuss how these results might have to be modified in light of our population diagram analysis, give a specific example, and discuss the effects of clumpiness.

6.1. Use of the Population Diagram

Results from the early spectral surveys of Linke et al. (1979) and Frerking et al. (1979) indicated that populations of a number of levels of several species were described by a single, but very low, excitation temperature. Although we have not analyzed the molecular species observed in these two investigations, we believe that their results can be satisfactorily explained in terms of subthermal excitation in a region of moderately high kinetic temperature, consistent with other information about the Sgr B2 molecular cloud (see, e.g., Lis & Goldsmith 1990). Working with a larger data base of molecular lines in the 3 mm wavelength range and using a rotation diagram analysis, Turner (1991) derived both rotation temperatures and molecular column densities. He also recognized the effect of saturation for some species. While some species could be fit with a single temperature, others required two temperature regimes if one assumed only a linear fit.

There have also been several extensive spectral line surveys at shorter wavelengths used to derive temperatures and densities using the rotation diagram approach. Serabyn & Weisstein (1995) studied SO, among many other species and found that analysis of the common ^{32}SO isotopomer, assuming optically thin emission, required that there be two different temperature components. However, observations of the less abundant ^{34}SO species indicated that some transitions of ^{32}SO were optically thick. The analysis of ^{34}SO was consistent with a single temperature and allowed these authors to determine the optical depths of transitions of the more abundant species. Adopting this correction, the ^{32}SO population diagram was consistent with a single temperature of 83 K, reasonably close to the 100 K derived from the ^{34}SO . This study clearly indicates the significance of optical depth effects, which may be considerably more widespread than can be immediately obvious from observations of a few transitions of a single isotopomer.

Sutton et al. (1995) analyzed numerous molecular transitions in the vicinity of the Orion-KL core and found that different species, as well as different isotopomers, gave significantly different temperatures when analyzed using the rotation diagram approach assuming optically thin LTE emission. These variations may be due to a significant extent to the effects of saturation in the more abundant species and to subthermal excitation as discussed above.

In their study of the disk-outflow system IRAS 20126+4104, Cesaroni et al. (1997) analyzed emission from transitions of CH_3CN and CH_3OH using a rotation diagram approach. In their analysis of the CH_3OH $J = 3 \rightarrow 2$ and $J = 5 \rightarrow 4$ transitions, these authors adopted a single-temperature optically thin fit to derive a rotation temperature of 50 K. However, inspection of their Figure 14 suggests that optical depth effects are likely playing a major

role in producing a systematic deviation from the expected linear $\ln(N_u/g_u)$ versus E_u relationship. In their analysis of CH_3CN data, a correction for saturation of the ground state lines was applied, which did have the effect of reducing the derived excitation temperature from 260 to 150 K.

Other uses of the population diagram approach have tended to focus on molecules with complex energy level structures and which in consequence have many accessible transitions in a limited frequency range. We note in this regard that the results of Blake et al. (1994) for SO_2 are suggestive of saturation producing systematic deviations from optically thin behavior, while the CH_3OH results of van Dishoeck et al. (1995) exhibit exactly the kind of scatter seen here in Figure 5. Bachiller et al. (1995) used CH_3OH to probe the young molecular outflow in L1157, and derived temperatures of 8 K for the ambient gas and 12 K for the outflow. We suggest that the significance of the temperature difference is limited by uncertain effects of saturation, which the restricted data set makes difficult to assess.

These examples indicate that close attention to the effects of saturation and non-LTE excitation as discussed here can serve only to increase our confidence in the molecular column densities and temperatures derived from multi-transition observations.

6.2. Analysis of Clumpy Regions

Most of the discussion so far has assumed that the source fills the beam. There are many cases, however, where this is not likely to be the case, and indeed molecular clouds are known to be very clumpy on all scales, with significant chemical inhomogeneities. For example, the early observations on Sgr B2 were made with spatial resolutions on the order of a parsec. It is unlikely that the trace molecules observed by Linke et al. (1979) and Frerking et al. (1979) fill the volume within the beam size used. If the emission is optically thin or if we can derive the optical depth correction factor, then the only uncertainty in using the population diagram approach is that the column density needs to be scaled upward by the factor $(\Delta\Omega_a/\Delta\Omega_s)$. The problem we face with emission from a clumpy or unresolved region is that the antenna temperatures (or intensities) are reduced by the beam dilution factor (or clump filling factor). Therefore we might detect weak emission with $T_A \ll T_{\text{kin}}$, and believe that the emission is optically thin. In the case where LTE applies, it is a simple matter to modify equation (24) to include a constant offset due to beam dilution,

$$\ln \frac{\gamma_u W}{g_u} = \ln N - \ln \left(\frac{\Delta\Omega_a}{\Delta\Omega_s} \right) - \ln C_\tau - \ln Z - \frac{E_u}{kT}. \quad (38)$$

As this beam filling factor does not change the shape of the population diagram curves, the analyses discussed above hold here. Independent observations are required to obtain an estimate of the molecular column density in the “filled” region, as distinguished from the beam-averaged column density that is obtained by assuming the dilution factor to be unity.

6.3. Application of the Population Diagram for Determination of Molecular Hydrogen Density

The discussion of § 5 indicates that there is well-defined behavior under non-LTE conditions that, in fact, makes the

population diagram an important technique for determining the density as well as the column density, if we have observations of transitions that are not thermalized. Here, we discuss in more detail an example applied to CS data in two giant molecular cloud cores obtained by Snell et al. (1984). This includes observations of the $2 \rightarrow 1$, $3 \rightarrow 2$, $5 \rightarrow 4$, and $6 \rightarrow 5$ transitions, having upper level energies between 7.1 and 49.6 K above the ground state. The Snell et al. (1984) data for the central positions of the sources S140 and NGC 2024 are plotted in Figure 9.

Several things are immediately evident from the plot. First, the points on the population diagram do fall fairly well on a straight line indicating an excitation temperature of close to 13 K. The transitions appear to be optically thin, which is consistent with conclusions of Mundy et al. (1986) based on observation of C^{34}S in the same sources. The excitation temperature of 13 K is far too low to really be indicative of LTE in the cores of these giant molecular clouds, so we see observational evidence for quasi-thermal excitation discussed in § 5 and the Appendix. The kinetic temperature in these regions can be determined using a variety of probes but is likely in the range 30–50 K. Model population diagrams for these two kinetic temperatures are shown in the left and right panels of Figure 9, respectively, for $5.75 \leq \log [n(\text{H}_2)/\text{cm}^{-3}] \leq 6.5$. We have adopted a line width of 2 km s^{-1} in accordance with the observations and fixed the CS column density to be $N(\text{CS}) = 1.09 \times 10^{14} \text{ cm}^{-2}$.

The population diagram analysis makes quite evident the manner in which the slope of the quasi-thermal excitation curves (inversely proportional to the more-or-less uniform excitation temperature of the transitions considered here) changes as a function of kinetic temperature and hydrogen density. We see a steady decrease in slope (increase in T_{ex}) as the hydrogen density increases, and also that a given H_2 density produces a smaller slope (larger excitation temperature) for a higher kinetic temperature. From Figure 9, we see that a density of $2 \times 10^6 \text{ cm}^{-3}$ gives good agreement with the slope of the data points for $T_k = 30 \text{ K}$, while a density of $0.6 \times 10^6 \text{ cm}^{-3}$ produces a comparably good fit for $T_k = 50 \text{ K}$. This column density has not been formally “best fit” but has been chosen to match the data reasonably well. From both panels of the figure, we see that $N(\text{CS})$ required is slightly smaller than 10^{14} cm^{-2} for both sources.

The analysis by Snell et al. (1984) fitted the antenna temperatures directly, treating the H_2 density and CS column density as independent variables, with the kinetic temperature determined independently. This approach does deal with the data directly, and the extent to which the model and the data agree or disagree is clearly evident. The results of the fitting by Snell et al. (1984) and those given here above are quite consistent. We do not feel that there should, in fact, be any systematic differences between the two approaches.

The population diagram approach offers the following quite clear advantages.

1. There is the possibility of recognizing optical depth effects directly from the form of the data, although this will, in general, require quite a large number of transitions spread over a range of upper state energies.
2. The appearance of quasi-thermal excitation immediately gives an independent lower limit to the kinetic temperature.

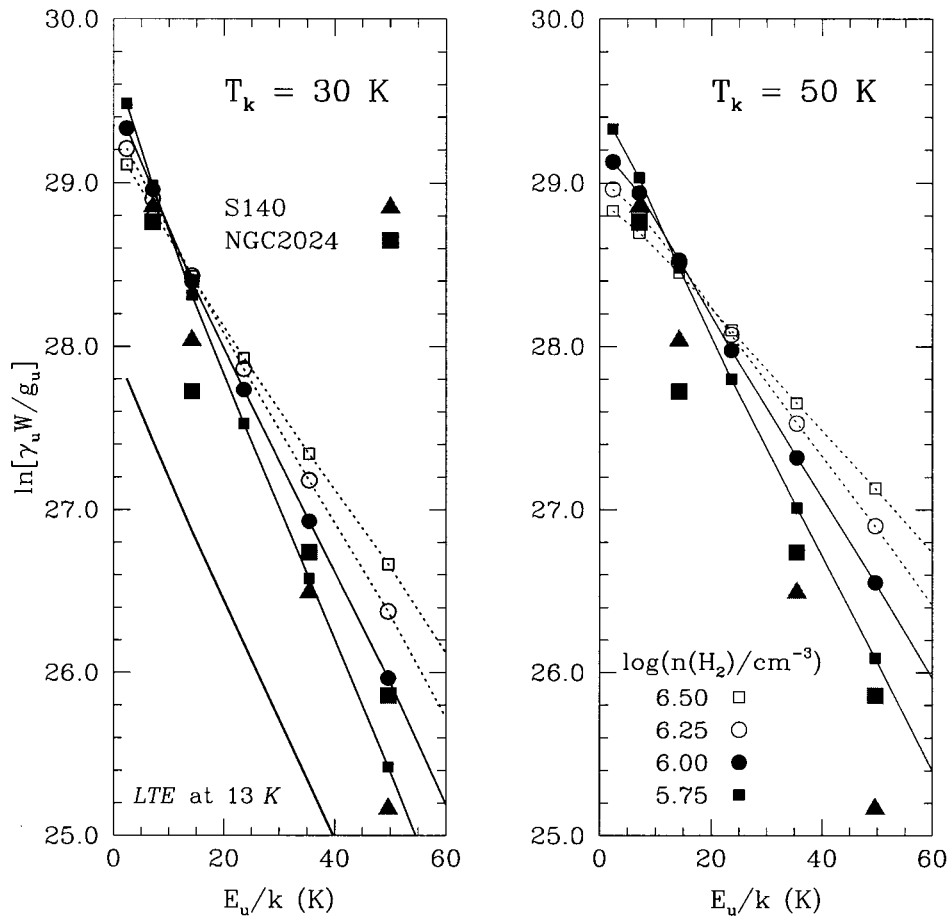


FIG. 9.—Population diagram analysis of multitransition CS data from Snell et al. 1984. Data from the (0, 0) position in sources S140 and NGC 2024 are plotted as large triangles and filled squares, respectively, while the results from different H_2 densities are indicated by symbols as defined in right panel. The slope of the population diagram for LTE at 13 K is indicated by the heavy curve in lower left panel. The results of model calculations at a kinetic temperature of 30 K are shown in the left panel, and for 50 K in the right panel. We have adopted a line width of 2 km s^{-1} in accordance with the observations, and the CS column density is $1.09 \times 10^{14} \text{ cm}^{-2}$ for all of the curves.

3. The trade-off between kinetic temperature and hydrogen density is quite evident, which is not at all the case when fitting unprocessed data directly.

4. If one can demonstrate that LTE does apply, then the kinetic temperature and the total molecular column density can be immediately obtained with good accuracy.

5. The ability to recognize the presence of multiple temperatures is a potential advantage but needs to be approached with caution in view of the concerns raised earlier about excitation and optical depth effects.

The population diagram and direct analysis methods both have the quality of being able to separate the effect of column density and space density changes. In view of its advantages and lack of any apparent drawbacks, there does not appear to be any reason not to use the population diagram approach for determination of physical conditions in dense clouds from multitransition molecular line data.

7. SUMMARY

We have examined in some detail the “rotation diagram” for analysis of multitransition molecular emission data, which we feel is better called the “population diagram” technique. In this approach, the natural logarithm of the integrated intensity of each transition

observed, multiplied by appropriate constants, is plotted against the energy of the upper level of the transition. The traditional use of this type of diagram has been to assume that the emission is optically thin and that LTE applies. In this limiting case, the integrated intensity is proportional to the upper level column density and the column densities are related by Boltzmann factors, so the locus of points on the population diagram should be a straight line, with slope proportional to the negative reciprocal of the temperature. A straightforward generalization of this technique to include the optical depth τ , and optical depth correction factor $C_\tau = \tau/(1 - e^{-\tau})$, but still assuming populations of all levels are in LTE at temperature T , gives the relationship

$$\ln \frac{\gamma_u W}{g_u} = \ln N - \ln C_\tau - \ln Z - \frac{E_u}{kT}, \quad (39)$$

where γ_u is the combination of constants relating integrated line intensity and upper level column density, N is the total molecular population, Z is the partition function, and E_u the upper state energy. We have derived the correction factor for linear molecules in LTE in analytic form and have used CH_3OH as representative of more complex molecules, to show how saturation can produce both systematic and apparently “scatter-like” deviations from optically thin behavior. These effects have been recognized to various degrees in papers in the literature, and we suggest that a

more systematic approach to consideration of saturation effects could improve reliability of molecular column density and temperature determinations.

We have examined the non-LTE behavior of linear molecules and have found that the apparent constancy of excitation temperature among levels with quite different spontaneous decay rates can be understood in terms of the frequency dependence of the quantities involved. As discussed in the Appendix, this quasi thermalization at an excitation temperature well below the kinetic temperature explains the apparently problematic results reported in the literature. We have also examined the population diagram as a technique to determine molecular hydrogen densities, which involves comparison of the form of the population diagram curves with statistical equilibrium/radiative trans-

fer code predictions. This approach appears to offer several important advantages compared to fitting intensities directly, including recognition of LTE, bounding the kinetic temperature, and clearly indicating the interrelated effects of the kinetic temperature and the excitation rate.

The National Astronomy and Ionosphere Center is operated by Cornell University under a cooperative agreement with the National Science Foundation. The research of W. D. L. was conducted at the Jet Propulsion Laboratory, California Institute of Technology, with support from NASA research grants. We thank L. Olmi and Å. Hjalmarson for carefully reading this paper and for helpful suggestions.

APPENDIX

QUASI-THERMAL EXCITATION

The curious behavior of the relative intensities, and hence the level populations of linear molecules discussed in §§ 5.1 and 6.3, deserves some further comment. The result suggested by Figure 6 is that the excitation temperature can remain relatively constant, or even increase, as the rotational quantum number J increases. This behavior is surprising because we know from equation (25) that the A -coefficients increase rapidly with increasing J , so that, in the case of subthermal excitation, we might think that the higher transitions are farther from thermalization, and hence their excitation temperatures should be lower. This proves not necessarily to be the case, however.

We can gain valuable insight into this question by examining initially a simplified version of the problem, which is just a two level system. However, it should be borne in mind that this analysis is also directly applicable to the case of a linear molecule provided that the collisions connect only successive levels, e.g., are “dipole collisions.” This behavior is not a precise description for most molecular species interacting with neutral collision partners, but we shall see that the behavior that is found shows many of the same characteristics derived from multilevel statistical equilibrium calculations using computed collision rates.

In the case of dipole collisions, as discussed by Goldsmith (1972), the relative populations of each pair of levels is decoupled from that of other levels. If we neglect the background radiation field, we obtain from the rate equations that the excitation temperature is given by the expression

$$T_{\text{ex}} = \frac{h\nu/k}{h\nu/kT_k + \ln(1 + A_{ul}/C_{ul})}. \quad (\text{A1})$$

Defining

$$\chi = \frac{A_{ul}}{C_{ul}} \quad (\text{A2})$$

and

$$K = \frac{h\nu}{kT_k}, \quad (\text{A3})$$

we obtain the simple and convenient expression

$$\frac{T_{\text{ex}}}{T_k} = \left[1 + \frac{1}{K} \ln(1 + \chi) \right]^{-1}. \quad (\text{A4})$$

χ and K can be considered independent variables that determine the T_{ex} as a fraction of T_k . The relationship is shown in Figure 10, in which the different sets of points correspond to different values of K , as a function of χ . We see that, for a given value of K , T_{ex} as a fraction of T_k increases monotonically as χ drops, which corresponds to moving closer to thermalization as the ratio of the collision rate to the spontaneous decay rate increases. For a fixed value of χ , T_{ex}/T_k increases as K increases. Thus, for a fixed ratio of spontaneous decay rate to collisional deexcitation rate, as the transition frequency relative to the kinetic temperature (both expressed as energies) increases, the excitation temperature relative to the kinetic temperature also increases. If we consider a fixed kinetic temperature, as the transition frequency increases, K increases, and thus so does the excitation temperature.

This behavior really reflects the definition of the excitation temperature in terms of a Boltzmann factor relating the upper and lower level populations (see eq. [18]). A fixed T_k and χ mean a fixed ratio of upward to downward transition rates, which from the basic definition of the rate equation translates to a fixed ratio of transition frequency to excitation temperature. Thus

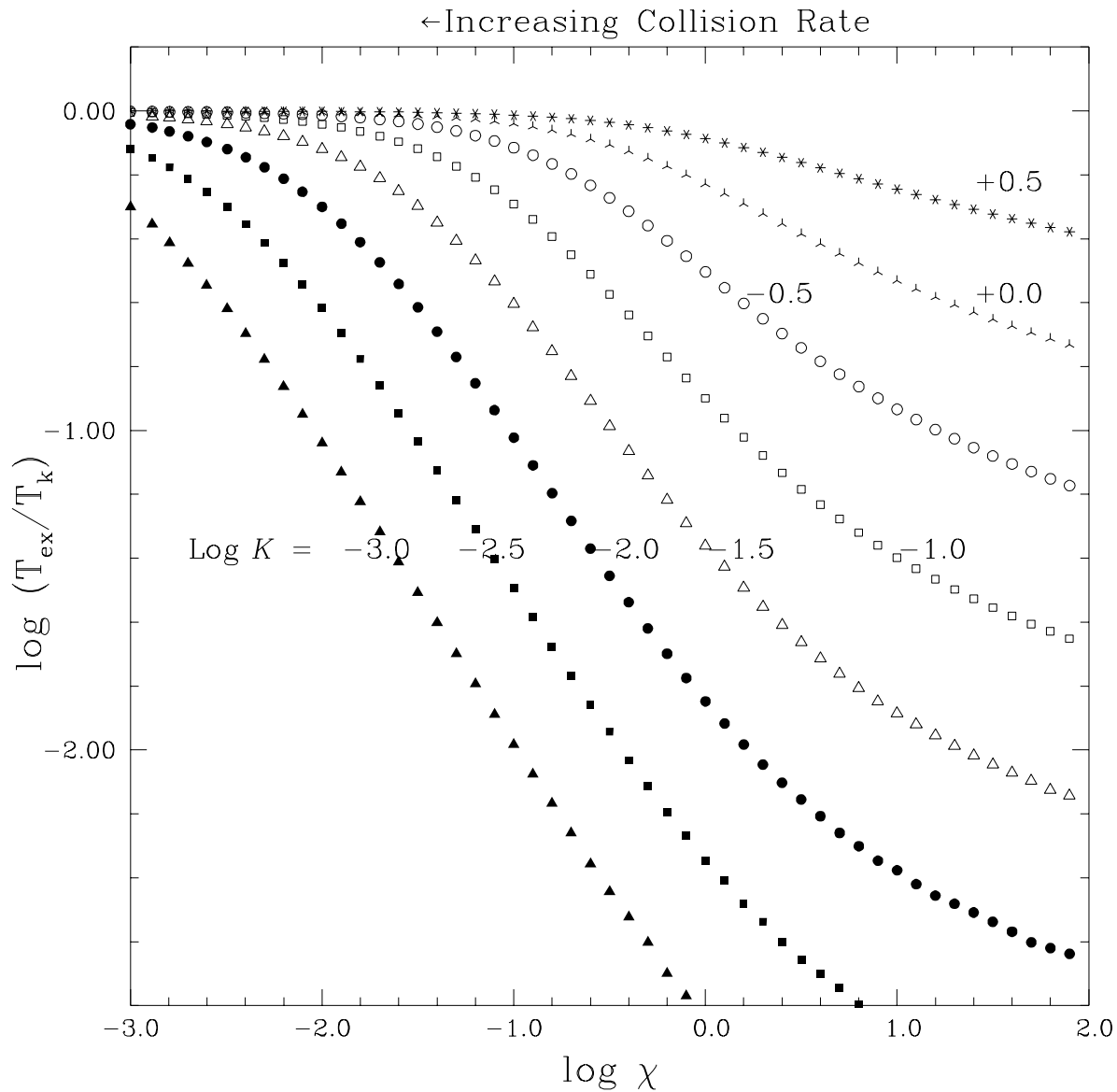


FIG. 10.—Solution of a two-level system in which the excitation temperature relative to the kinetic temperature is calculated as a function of the parameters $\chi = A_{ul}/C_{ul}$, the ratio of spontaneous to collisional deexcitation rates, and $K = E_{ul}/kT_k$, the ratio of the energy difference of the transition to the energy corresponding to the kinetic temperature. There is no background radiation considered in this calculation, which also assumes the transition optically thin.

a greater transition frequency requires a higher excitation temperature to achieve the same ratio of level populations, and vice versa.

If we consider the situation with the transition frequency fixed, as the kinetic temperature is increased, K decreases, but the fact that T_{ex}/T_k rises in consequence does not immediately indicate what happens to the excitation temperature itself. If we consider the limit $h\nu \ll kT_k$, for χ not too small (i.e., if we are not too close to LTE), equation (A4) becomes

$$T_{ex} = \frac{h\nu/k}{\ln(1 + \chi)}. \quad (\text{A5})$$

We see that, in this limit, the excitation temperature is independent of the kinetic temperature. Thus the sets of points for different values of $\log K$ at a fixed χ , which are separated by 0.5 dex, give values of $\log(T_{ex}/T_k)$ that differ by this same factor.

The situation for a linear molecule with a “ladder” of transitions is somewhat more involved. As the frequency and spontaneous decay rate both depend on the transition in question, K and χ are not independent variables. Knowing the variation of frequency and spontaneous decay rate as a function of J , it is possible to see how the various transitions of a linear molecule are located in Figure 10. It is more convenient, however, to express K and χ in terms of parameters that characterize the $J = 1 \rightarrow 0$ transition, through

$$K = K_1 J \quad (\text{A6})$$

and

$$\chi = \chi_1 \frac{3J^4}{2J+1}, \quad (\text{A7})$$

where

$$K_1 = \frac{h\nu_{10}}{kT_k} \quad (\text{A8})$$

and

$$\chi_1 = \frac{A_{10}}{C_{10}}. \quad (\text{A9})$$

We assume that all transitions are characterized by equal deexcitation rates, which is reasonably close to what is found from realistic calculations of cross sections.

The calculation of the excitation temperature as a function of K_1 , χ_1 , and J is shown in Figure 11. We now see something quite different as we move up the rotational “ladder”: for a wide range of conditions T_{ex}/T_k is essentially independent of J . Note in particular that for values of χ_1 between 0.01 and 0.10, the quasi independence of excitation temperature of J starts at quite modest values of J , between 5 and 10. As an example, CS at a kinetic temperature of 23 K corresponds to $K_1 = 0.1$, and we see that transitions for J greater than a few are predicted to have an excitation temperature of about 8 K

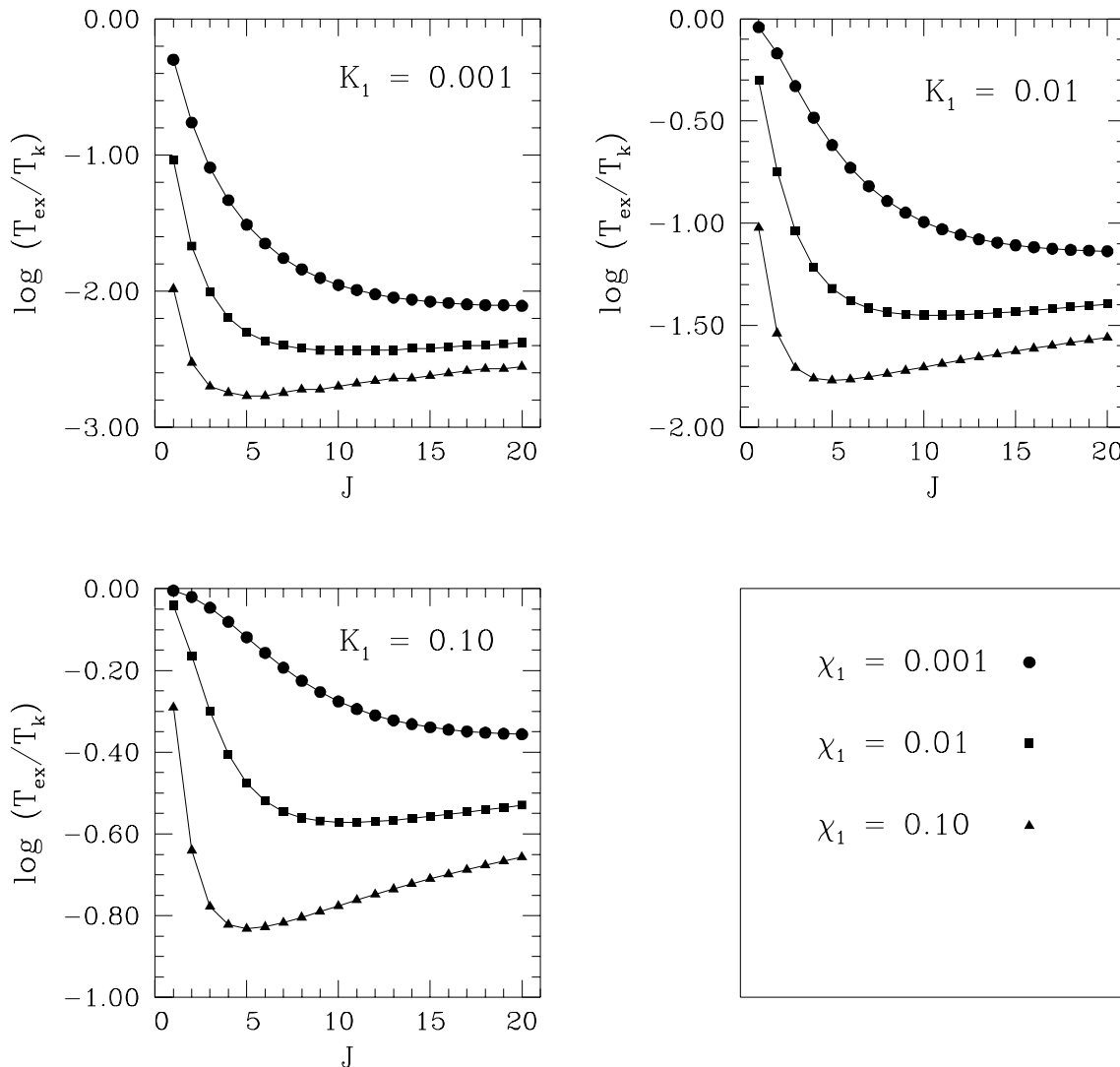


FIG. 11.—Excitation temperature for different transitions of a linear molecule with collisional excitation by dipole collisions ($\Delta J = \pm 1$). The parameters χ_1 and K_1 apply to the $1 \rightarrow 0$ transition and define the ratios of the spontaneous to collisional deexcitation rate and the energy of the transition to that of the kinetic temperature, respectively. For significant ranges of J as well as of the parameters defining the conditions in which the molecules are found, the excitation temperature is essentially independent of J .

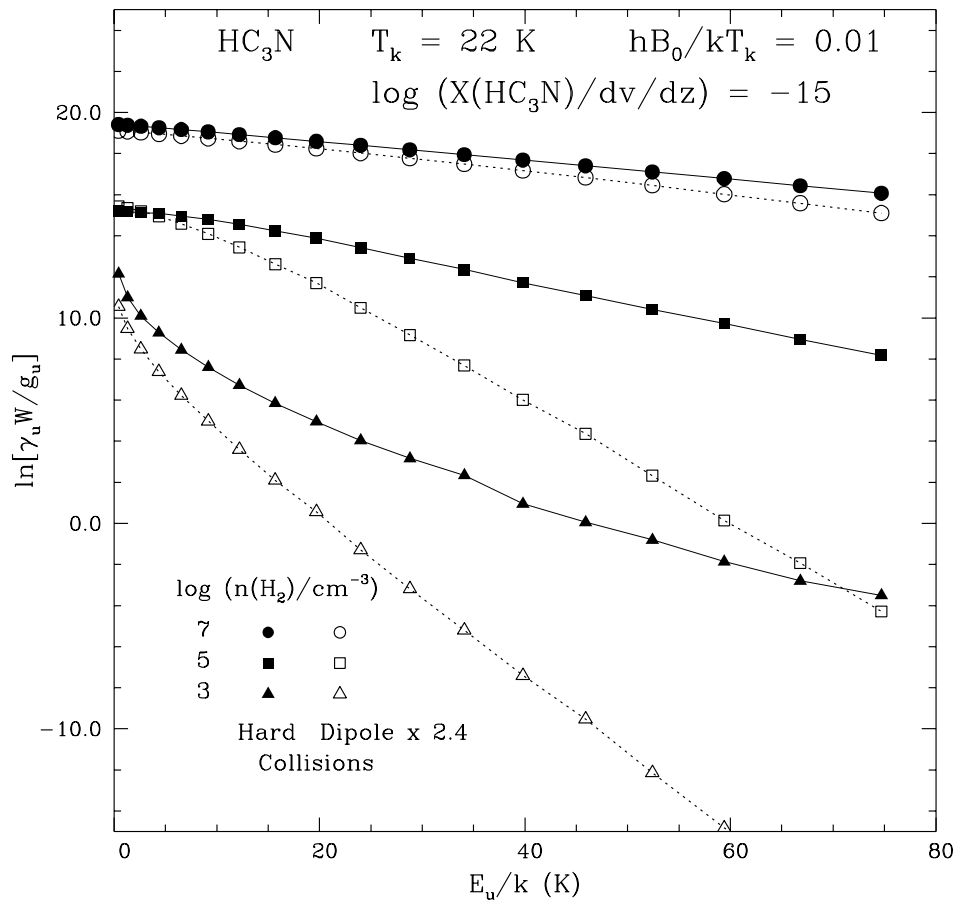


FIG. 12.—Comparison of population diagrams for HC_3N assuming different excitation models. The solid curves are for “hard” collisions, which reflect realistic intermolecular forces and which allow changes in the rotational quantum number to take place with substantial probability for ΔJ up to 10. The dotted curves are for dipole collisions, in which $\Delta J = \pm 1$. The hard collisions produce significantly greater excitation of the higher J transitions for hydrogen densities $\leq 10^5 \text{ cm}^{-3}$ than do the dipole collisions. The conditions are otherwise the same as described for Fig. 6.

for $\chi_1 = 0.01$. Taking a collision rate coefficient of $2 \times 10^{-11} \text{ cm}^3 \text{ s}^{-1}$, we find that this corresponds to a density of 10^7 cm^{-3} . In a basic sense, dipole collisions can produce excitation temperatures that are largely independent of J .

The quasi-thermal behavior with $T_{\text{ex}} < T_k$ is emphasized by the form of the actual collision cross sections. This point is addressed in Figure 12, which compares the population diagrams obtained for the standard “hard” collisions with those from “dipole” collisions. These calculations were carried out including the 2.7 K background radiation field. The abundance of HC_3N is sufficiently low that all transitions are optically thin. The deexcitation rates from Green & Chapman (1978) allow $-10 \leq \Delta J \leq 0$ with significant probability, and $-20 \leq \Delta J \leq 0$ with nonzero probability. For dipole collisions, we restrict the nonzero deexcitation rates to transitions with $\Delta J = -1$ but multiply these rates by a scaling factor such that the deexcitation rate is the same as the total deexcitation rate for hard collisions. This factor is found to be approximately 2.4 for initial J greater than a few and closer to unity for smaller initial J . We see for the dipole collisions that there is significantly lower excitation of the higher J levels. For $n(\text{H}_2) = 10^3 \text{ cm}^{-3}$, the excitation temperature is 2.7 K (close to the background temperature), compared to 5 K for the hard collisions. For $n(\text{H}_2) = 10^5 \text{ cm}^{-3}$, the excitation temperatures produced by the scaled dipole collisions are about 3.3 K, compared to 8 K for the hard collisions. For densities $\geq 10^7 \text{ cm}^{-3}$ all transitions are thermalized for scaled dipole collisions. For the case of HC_3N considered here, we have found that realistic collisional cross sections, which produce a large change in J , result in values of T_{ex} that are significantly above the background temperature and are also essentially independent of J . This behavior presumably applies to other linear molecules, and very similar behavior for the symmetric top molecule CH_3CN was discussed by Linke et al. (1982). Thus, the expectation that excitation temperatures necessarily drop as one moves up an energy level diagram with gradually increasing spontaneous decay rates must be recognized to be incorrect.

REFERENCES

- Askne, J., Höglund, B., Hjalmarson, Å., & Irvine, W. M. 1984, *A&A*, 130, 311
- Bachiller, R., Liechti, S., Walmsley, C. M., & Colomer, F. 1995, *A&A*, 295, 51
- Bergin, E. A., Goldsmith, P. F., Snell, R. L., & Ungerechts, H. 1994, *ApJ*, 431, 674
- Blake, G. A., van Dishoeck, E. F., Jansen, D. J., Groesbeck, T. D., & Mundy, L. G. 1994, *ApJ*, 428, 680
- Cesaroni, R., Fell, M., Testi, L., Walmsley, C. M., & Olmi, L. 1997, *A&A*, 325, 725
- Frerking, M. A., Linke, R. A., & Thaddeus, P. 1979, *ApJ*, 234, L143
- Goldsmith, P. F. 1972, *ApJ*, 176, 597
- Green, S., & Chapman, S. 1978, *ApJS*, 37, 169
- Kraus, J. D. 1982, *Radio Astronomy* (rev. ed.; Powell, OH: Cygnus-Quasar)
- Lafferty, W. J., & Lovas, F. J. 1978, *J. Phys. Chem. Ref. Data*, 7, 441
- Linke, R. A., Cummins, S. E., Green, S., & Thaddeus, P. 1982, in *Regions of Recent Star Formation*, ed. R. S. Roger & P. E. Dewdney (Dordrecht: Reidel), 391
- Linke, R. A., Frerking, M. A., & Thaddeus, P. 1979, *ApJ*, 234, L139
- Lis, D. C., & Goldsmith, P. F. 1990, *ApJ*, 356, 195
- Loren, R. B., & Mundy, L. G. 1984, *ApJ*, 286, 232
- Mundy, L. G., Snell, R. L., Evans, N. J., II, Goldsmith, P. F., & Bally, J. 1986, *ApJ*, 306, 670
- Nummelin, A., Dickens, J. E., Bergman, P., Hjalmarson, Å., Irvine, W. M., Ikeda, M., & Ohishi, M. 1998, *A&A*, 337, 275
- Olmi, L., Cesaroni, R., & Walmsley, C. M. 1993, *A&A*, 276, 489
- . 1996, *A&A*, 307, 599
- Peng, R. S., & Whiteoak, J. B. 1993, *MNRAS*, 260, 529
- Serabyn, E., & Weisstein, E. W. 1995, *ApJ*, 451, 238
- Snell, R. L., Mundy, L. G., Goldsmith, P. F., Evans, N. J., II, & Erickson, N. R. 1984, *ApJ*, 276, 625
- Sutton, E. C., Peng, R., Danchi, W. C., Jaminet, P. A., Sandell, G., & Russell, A. P. G. 1995, *ApJS*, 97, 455
- Turner, B. E. 1991, *ApJS*, 76, 617
- van Dishoeck, E. F., Blake, G. A., Jansen, D., & Groesbeck, T. D. 1995, *ApJ*, 447, 760